

## New impact-melt rock from the Roter Kamm impact structure, Namibia: Further constraints on impact age, melt rock chemistry, and projectile composition

Lutz HECHT<sup>1\*</sup>, W. Uwe REIMOLD<sup>1</sup>, Sarah SHERLOCK<sup>2</sup>, Roald TAGLE<sup>1</sup>,  
 Christian KOEBERL<sup>3</sup>, and Ralf-Thomas SCHMITT<sup>1</sup>

<sup>1</sup>Museum for Natural History, Humboldt University, Invalidenstrasse 43, 10115 Berlin, Germany

<sup>2</sup>Department of Earth and Environmental Sciences, Centre for Earth, Planetary, Space and Astronomical Research (CEPSAR),  
 The Open University, Milton Keynes, MK7 6AA, UK

<sup>3</sup>Center for Earth Sciences, University of Vienna, Althanstrasse 14, A-1090 Vienna, Austria

\*Corresponding author. E-mail address: [lutz.hecht@museum.hu-berlin.de](mailto:lutz.hecht@museum.hu-berlin.de)

(Received 29 October 2007; revision accepted 20 December 2007)

---

**Abstract**—A new locality of in situ massive impact-melt rock was discovered on the south-southwestern rim of the Roter Kamm impact structure. While the sub-samples from this new locality are relatively homogeneous at the hand specimen scale, and despite being from a nearby location, they do not have the same composition of the only previously analyzed impact-melt rock sample from Roter Kamm. Both Roter Kamm impact-melt rock samples analyzed to date, as well as several suevite samples, exhibit a granitic-granodioritic precursor composition. Micro-chemical analyses of glassy matrix and Al-rich orthopyroxene microphenocrysts demonstrate rapid cooling and chemical disequilibrium at small scales. Platinum-group element abundances and ratios indicate an ordinary chondritic composition for the Roter Kamm impactor. Laser argon dating of two sub-samples did not reproduce the previously obtained age of  $3.7 \pm 0.3$  (1 $\sigma$ ) for this impact event, based on <sup>40</sup>Ar/<sup>39</sup>Ar dating of a single vesicular impact-melt rock. Instead, we obtained ages between 3.9 and 6.3 Ma, with an inverse isochron age of  $4.7 \pm 0.3$  Ma for one analyzed sub-sample and  $5.1 \pm 0.4$  Ma for the other. Clearly a post-5 Ma impact at Roter Kamm remains indicated, but further analytical work is required to better constrain the currently best estimate of 4–5 Ma. Both impactor and age constraints are clearly obstructed by the inherent microscopic heterogeneity and disequilibrium melting and cooling processes demonstrated in the present study.

---

### INTRODUCTION

The 2.5 km diameter Roter Kamm impact crater is located at 27°45'58"S/16°17'17"E in the southern Namib desert (Fig. 1). The structure is mostly covered by desert sand. Only along the crest of the crater rim does one find sporadic outcrop of target rocks that belong to the Namaqualand Metamorphic Complex and the Gariiep Group (see Reimold and Miller 1989; Reimold et al. 1994). The impact origin of this crater structure was already suggested in the 1970s (e.g., Fudali 1973), but was only confirmed through the discovery of shock-metamorphosed rocks by Reimold and Miller (1989; see also Reimold et al. 1997). Koeberl et al. (1993) obtained a  $3.7 \pm 0.3$  Ma <sup>40</sup>Ar/<sup>39</sup>Ar step-heating age for a single sample of impact-melt rock. Further geophysical, mineralogical, and chemical investigations on this impact structure were given by Koeberl et al. (1989), Degenhardt et al. (1994, 1996), Brandt et al. (1997), and Grant et al. (1997).

Most recently, Reimold et al. (1997) reported the first observation of suevitic impact breccia at a locality on the western crater rim (Fig. 1, RK95/17). These suevite blocks had previously not been accessible due to extensive sand cover of this site. Shifting wind directions on occasion uncover previously unknown outcrops. Reimold et al. (1997) observed that these breccias contained very few (<<1 vol%) impact-melt fragments. This general lack of impact melt at Roter Kamm is surprising, as the target stratigraphy includes a significant component of crystalline basement rocks, including granitic to granodioritic gneiss, with xenoliths of other felsic and mafic lithologies (including granulites), and extensive occurrence of quartz and quartz-feldspar veins and pegmatitic pods (Reimold and Miller 1989; Reimold et al. 1994). It is, of course, possible that there are extensive melt rock occurrences within the crater fill, and that any melt rock ejecta were removed by erosion since crater formation. In several places outside of, and in a few places on top of, the crater rim have these authors observed remnants of

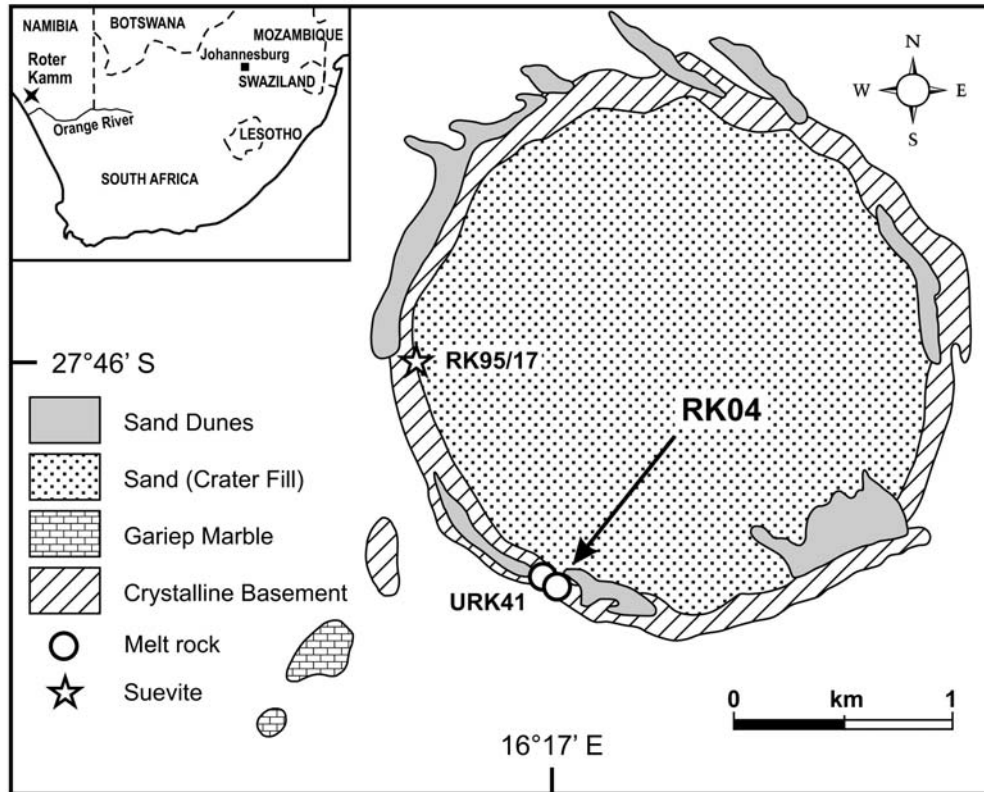


Fig. 1. Geological sketch map of Roter Kamm indicating sample localities of melt rock and suevite (modified from Reimold et al. 1997). Apart from the new melt rock occurrence RK04 the location of melt rock sample URK41 (Reimold and Miller 1989; Reimold et al. 1994) and suevite samples at RK95/17 (Reimold et al. 1997) are indicated.

sedimentary cover strata. This involves mostly marble of the Gariiep Group (Fig. 1), but very small exposures of sandstone have also been observed. It is not known how thick the sedimentary cover was at the time of the impact, but it was probably not very thick. The work of Grant et al. (1997) suggested that degradation of this relatively young impact crater was likely of the order of several tens of meters, allowing for remnants of impact breccia ejecta possibly still occurring on top of and outside of the crater rim (Reimold et al. 1997).

Previous work has shown that the crater was essentially excavated in crystalline basement. By analogy to other impact structures formed in crystalline rock, significant amounts of impact melt should have been generated. And yet, despite a number of expeditions that investigated regularly the entire crater rim, previously only a single impact-melt rock sample (URK41 described by Reimold and Miller 1989; Koeberl et al. 1993, and Degenhardt et al. 1996) had been found (Fig. 1).

As recently reviewed by Rajmon et al. (2005), earlier dating efforts of Roter Kamm samples (Koeberl et al. 1993) yielded a  $1292 \pm 49.5$  Ma (ages quoted here with 1 sigma errors) whole-rock Rb-Sr age, which was interpreted as coincident with Namaqualand metamorphism, and ages of 671 Ma and  $466 \pm 15.5$  Ma for whole rock and mineral fractions of two other samples. These dates correlate with Damara magmatic activity and/or metamorphic overprint on older basement. K-Ar ages of  $464 \pm 21$  Ma and  $479 \pm$

$22$  Ma, and  $251 \pm 12$  and  $255 \pm 12$  Ma were also obtained by Koeberl et al. (1993) for several breccia samples that initially had been classified as possible "pseudotachylite" by Reimold and Miller (1989), but later were revealed by Degenhardt et al. (1994, 1996) as cataclasites. Apatite fission-track ages by Koeberl et al. (1993) of 20–28 Ma, were related by these authors to the Burdigalian peneplanation at 25 Ma or partial impact resetting. Onstott et al. (1986) reported a  $342 \pm 4$  Ma  $^{40}\text{Ar}/^{39}\text{Ar}$  step-heating plateau age for plagioclase from about 200 km southeast of Roter Kamm and related this to Karoo magmatic activity. Likewise, Rajmon et al. (2005) obtained several  $^{40}\text{Ar}/^{39}\text{Ar}$  step heating plateau ages, as well as total degassing ages, in the range from 255 to 323 Ma, besides two 74.4 and 78.8 Ma ages, for various specimens from a breccia and host rock pair. Rajmon et al. (2005) suggested that these results related to a thermal event in the carboniferous, but that further partial argon loss was incurred at 3.7 Ma as a result of the impact event. They confirmed that the Roter Kamm breccias were cataclasites and did not experience heating above about 290 °C.

During a two-day field trip to the Roter Kamm impact structure by two of us (UR and LH) in April 2004, an in situ occurrence of impact-melt rock was discovered on the south-southwestern crater rim. In order to better constrain the impact age, melt rock composition, and projectile origin, we present a mineralogical,

petrographic, and chemical study including  $^{40}\text{Ar}/^{39}\text{Ar}$  geochronology.

### SAMPLES AND ANALYTICAL METHODS

The new melt rock occurrence was recognized by an abundance of up to 5 cm sized pebbles of black vesicular material on the desert sand. It was found that only a centimeter to decimeter thick cover of sand occurred at this site. Below, a coherent mass of black, homogeneous looking rock was found (Figs. 2a and 2b). The limited time available for exploration during field work only allowed to uncover an area of about  $2 \times 1$  m and to take a small number of samples exclusively from the uppermost decimeter of this occurrence. It is thought that erosion due to shifting wind patterns excavated this site, which had been traversed on previous visits to the crater without providing a hint at the existence of this melt rock.

Three main samples and several sub-samples were prepared for whole rock analysis. Four polished thin sections were studied by polarization microscopy. A scanning JEOL JSM 6300 electron microscope (SEM) equipped with a RÖNTEC energy-dispersive analytical system including Quantax software was used for imaging and qualitative analyses of minerals. Electron microprobe analysis on glass and minerals was performed on a Jeol JXA-8800 operating at 15 kV and 15 nA. Analyses were calibrated using Smithsonian international mineral standards (Jarosewich et al. 1980). Counting times were 20 s on peak and 10 s on background. For analysis on the glass matrix the electron beam was defocused to a diameter of 5  $\mu\text{m}$ . The reproducibility of test measurements on standards was generally much better than 3 rel% (one sigma), except for values closer to the detection limit (generally values below 0.2 wt%), where the reproducibility may be reduced to about 10 rel%.

Whole rock chemical analyses for major and some trace elements were carried out by X-ray fluorescence spectroscopy (XRF) at the Institute of Geochemistry, University of the Witwatersrand, Johannesburg (samples RK04/3-1, 3-2) and at the Museum of Natural History, Berlin (samples RK04/3-3, 5, 6). Details of the analytical procedures and accuracies are the same as those described by Reimold et al. (1994) and by Schmitt et al. (2004) for the samples analyzed at the University of Witwatersrand and at the Museum of Natural History, respectively.

Trace element contents were determined by instrumental neutron activation analysis (INAA) at the University of Vienna. Analytical techniques, standards, instrumentation, data correction, and information on accuracy and precision, are described in detail by Koeberl (1993) and Son and Koeberl (2005). The iridium content was determined by multi-parameter coincidence spectrometry after neutron irradiation (for details, see Koeberl and Huber 2000).

Platinum group element (PGE) analyses were carried out by nickel-sulfide (NiS) fire-assay pre-concentration combined with ICP-MS analysis, following the procedure

described by Plessen and Erzinger (1998) and Tagle and Claeys (2005). Several aliquots of three melt-rock samples were analyzed independently. The pre-crushed sample aliquots from sample RK04/3, sub-labelled as RK04/3-1 and RK04/3-2, were milled using an agate mill. Aliquots of the other samples were crushed using a corundum ball mill as described by Tagle and Claeys (2005). The PGE solutions (10 ml) obtained after the NiS fire-assay pre-concentration (sample aliquots used for each analyses are given in Table 4) were measured by ICP-MS independently on two separate days. The resultant concentrations were averaged and the range of the two analyses was used to estimate the uncertainties for each element according to the method followed by Tagle and Claeys (2005).

Two sub-samples (RK04/3A and RK04/3B) were prepared for  $^{40}\text{Ar}/^{39}\text{Ar}$  dating as 5-mm-thick slabs, of which 200–300  $\mu\text{m}$  thick polished sections were prepared. Sections of these slabs, selected because they seemed to contain relatively few clasts, were lifted off the glass slide and ultrasonically cleaned using methanol and de-ionized water. The chosen sections were wrapped in aluminum foils and irradiated at the McMaster Nuclear Reactor, Canada, for 16 hours, together with the biotite standard GA1550 ( $98.79 \pm 0.96$  Ma; Renne et al. 1998) to monitor neutron flux. The calculated J value was 0.000134 with an assigned 0.5% error, which is included in the reported age data. Interfering reactions arising during irradiation were corrected using the following correction factors:  $^{39}\text{Ar}/^{37}\text{Ar} = 0.00065 \pm 0.0000033$ ,  $^{36}\text{Ar}/^{37}\text{Ar} = 0.000264 \pm 0.0000013$ ,  $^{40}\text{Ar}/^{39}\text{Ar} = 0.0085 \pm 0.0$ , and a mass discrimination value of 283. Samples were analyzed using the infrared laser probe step-heating technique, as outlined in Kelley and Gurov (2002). All step-heating spectra and inverse isochron correlation diagrams, and weighted mean ages, were calculated using Isoplot 3 (Ludwig 2002).

## RESULTS

### Petrography and Mineral Chemistry

Although the melt rock appears rather homogeneous at the outcrop scale, it is heterogeneous at the centimeter and microscopic scales (Fig. 2c). The melt rock can be clast-poor or clast-rich, and can be composed of relatively wide (i.e., at the millimeter scale) areas that are either glassy or devitrified, with low or high density of microlites (Fig. 2d). There can be variable loads of clasts, and areas with either a rather well-stratified (banded) schlieren texture or others with a true (slag-like) melange of swirls of glass/melt. Also the distribution and density of vesicles within samples is vastly different from area to area. Vesicle sizes also vary from several millimeters to some microns (Fig. 2). It is obvious that specific glass areas that have high abundances of tiny vesicles must have formed from volatile-rich precursor minerals.

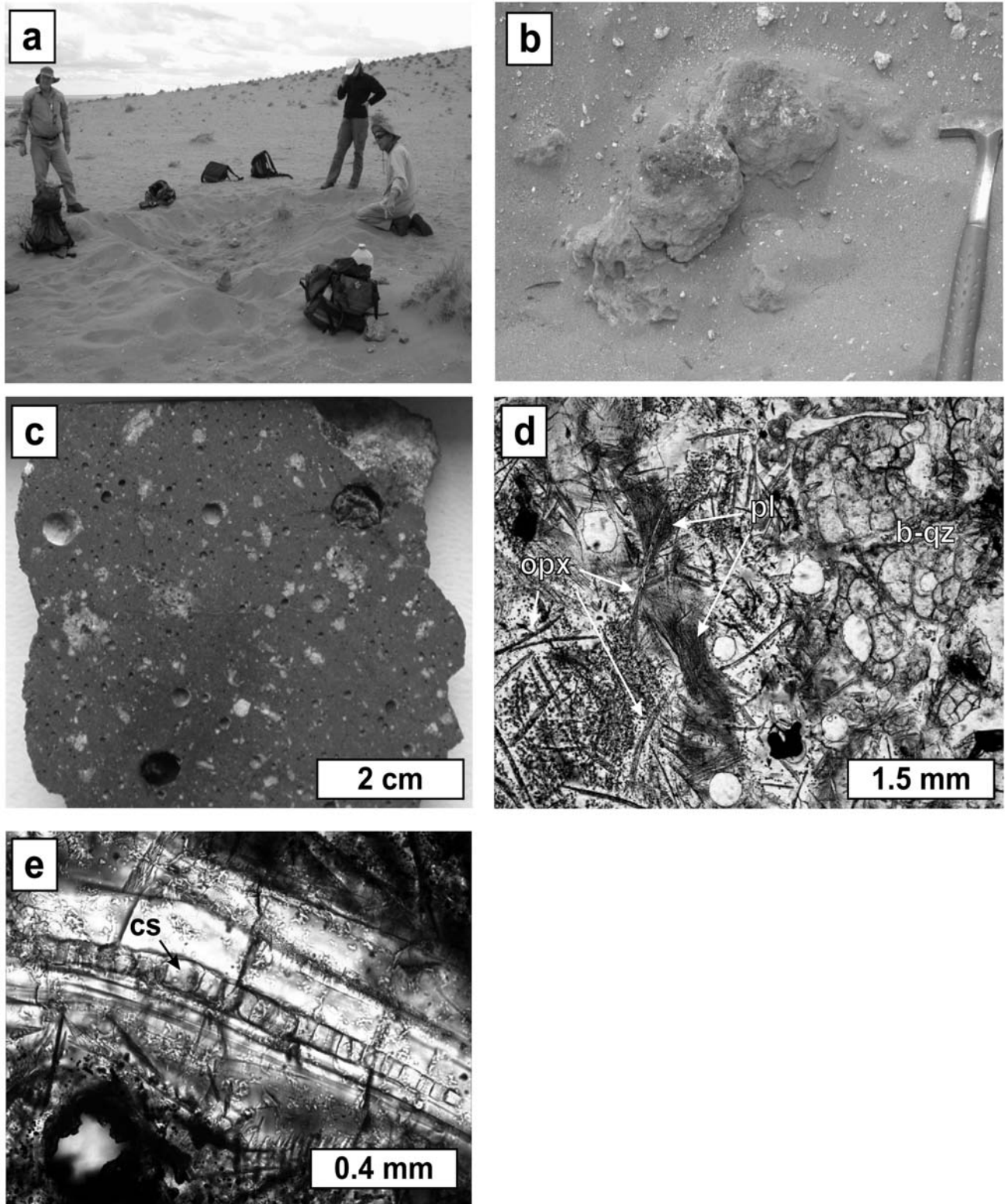


Fig. 2. a) Excavation of a  $2 \times 1$  meter outcrop of melt rock occurrence. b) Detail of melt rock outcrop showing a rough surface and abundant vesicles. c) Polished cut of melt rock hand specimen RK04/3 with sub-cm mineral clasts and vesicles. d) Thin section images of melt-rock sample RK04/3 with abundant plagioclase (pl) and orthopyroxene (opx) microphenocrysts. One part of a several millimeters large ballen quartz clast (b-qz) is shown on the right side of the image. e) Thin section image of a detail from a lechatelierite clast with inclusions of coesite (cs).

Vesicle-bearing clasts of lechatelierite have also been observed. Most vesicles are empty, but a few are filled with carbonate or brownish masses of phyllosilicate, and a few others have an inner lining of clear glass. Overall, the melange material does seem to be—at least in part—an agglomeration of individual glass/melt volumes, sometimes clearly separated from each other by narrow (<20  $\mu\text{m}$ ) seams.

The different coloration of matrix areas can, in places, be directly linked to the local occurrence of mineral or lithic inclusions that are relics of largely melted precursor material. This includes clasts of feldspar and feldspar-quartz aggregates, as well as mixtures of felsic and mafic minerals, with biotite likely being the most important mafic mineral phase. All mafic material is either melted or oxidized. Patches of black material, likely composed of Fe and Ti oxides, are interpreted as remains of biotite decomposition. Some dark brownish clasts represent a fluidal-textured mass of tiny, lath-like biotite crystals, suggesting that these clasts are derived from recrystallization of fully melted biotite. K-feldspar (orthoclase and microcline) and plagioclase relics have been noted, with plagioclase only forming a subordinate proportion mostly within clasts that are still recognizable as granitoid-derived. No shocked plagioclase crystals were observed. Quartz and feldspar mineral clasts are abundant (estimated at about 5–10 vol% in clast-poor areas, up to >30% in clast-loaded areas), and often formed the nuclei for microlite growth. We have observed clasts of unshocked feldspar, although these are rare. Some of the silica nuclei are composed of two phases, one of which has a higher refractive index than the other. The fact that radial fractures sometimes emanate from such occurrences is suggestive of volume increase due to the partial back-transformation of a high-pressure polymorph to  $\alpha$ -quartz. Chains of box-like, in part near-isotropic microcrystals also likely represent coesite crystallized from (surrounding) lechatelierite (Fig. 2e). Many quartz clasts are unshocked, but a significant percentage has been converted to diaplectic glass or lechatelierite. Diaplectic feldspar glass also occurs, but is comparatively rare. Some partially melted lithic clasts comprise crystalline relic grains, diaplectic glass, and fused glass (including lechatelierite and feldspathic glass, as determined by SEM analysis). In addition, annealing of clasts is not abundant but occurs scattered throughout these melt materials—indicating that peak temperatures have been highly variable on the microscopic scale. Fully annealed quartzitic clasts indicate that temperatures on the order of 1500 °C were attained at least locally. A small number of 0.5 to 2 cm sized granitic clasts have been sampled, all of which experienced a wide range of shock deformation and associated temperature effects. This ranges from unshocked crystals to partial and complete melting of both felsic and mafic minerals—all occurring in the same lithic clast. Individual mineral grains may also be partially or even completely annealed—attesting to the local temperature gradients after shock deformation. This is also observed for ballen quartz particles that are thought to represent converted

diaplectic quartz glass or lechatelierite (Stöffler and Langenhorst 1994). After ballen formation, such grains were partially or completely annealed—whereby the ballen rims can still be recognized. Unaltered ballen quartz is somewhat more prominent than quartz clasts with PDFs.

Quartz clasts with planar fractures are rare. The typical patterns of short shock fractures are more frequently observed, are of irregular geometry but often occurring in distinct fashion, such as marking an apparent cleavage (i.e., at roughly 90 degrees to their orientations), emanating from a focal point in radial fashion, or in a fan-like arrangement. These features are indicative of a <10 GPa shock degree. PDFs have been noted but are very rare compared to the other shock deformation effects. A single quartzite clast (derived from Gariep metasediment cover of the target area; Reimold and Miller 1989) contains several microscopic quartz crystals with up to 2 sets of PDFs. A single, ~0.3 mm wide quartz crystal was noted with a high density of PDFs in numerous orientations, to the effect that the grain has lost much of its original birefringence and is close to isotropization. A large number of quartz grains appear toasted—with strongly reduced birefringence and a weak brownish coloration, but lacking in PDFs, although some of these grains do have high densities of shock fractures. A few crystals of relatively high refractive index have been noted that could represent apatite or tourmaline; no zircon crystals were evident. These crystals appear somewhat annealed, so that it is difficult to identify these minerals by normal optical observation.

Sample RK04/3 has the lowest clast content. It is mainly composed of variably colored schlieren or sectors of glass that form a generally chaotic mix of three types of glasses, a) the main bright glass matrix, b) brownish glassy patches, and c) lechatelierite. The main glass matrix or brownish glass patches show incipient crystallization of microlites with up to a few micrometer thickness and up to several tens of micrometers in length. The acicular or whisker-like microlites are composed of plagioclase and orthopyroxene and amount up to approximately 20 vol% of the melt rock. Plagioclase microlites are commonly skeletal. Frequently they form dense feathery aggregates (Figs. 2d and 3). Plagioclase ranges in composition from  $\text{An}_{35}$  to  $\text{An}_{50}$  and is, on average, of andesine composition (Table 1). Acicular orthopyroxene is either irregularly distributed within the glass matrix or may radiate around xenocrysts (e.g., quartz grains). The overall composition of orthopyroxene is rather homogeneous (Table 1); however, there is a slight decrease in  $X_{\text{Mg}}$  from crystal cores ( $X_{\text{Mg}} = 0.80$ ) to rims ( $X_{\text{Mg}} = 0.75$ ), which most likely indicates a temperature decrease during crystal growth (e.g., Montel and Vielzeuf 1997). Note the rather high Al content of orthopyroxene. Al-rich orthopyroxenes of similar composition have been previously reported from impact-melt breccias, e.g., from the Ries crater (Engelhardt et al. 1995), and from high-grade terrestrial rocks (Villasca et al. 2007 and references therein). Partial melting experiments of crustal

Table 1. Averages of electron microprobe analyses, mineral formula, and mineral end members for plagioclase (Pl) and orthopyroxene (Opx) in Roter Kamm impact-melt rock sample RK04/3.

	Pl (n = 18)			Opx (n = 9)	
		sd			sd
SiO <sub>2</sub> wt%	58.75	1.60	SiO <sub>2</sub> wt%	49.30	0.69
TiO <sub>2</sub>	0.05	0.04	TiO <sub>2</sub>	0.27	0.05
Al <sub>2</sub> O <sub>3</sub>	25.92	1.09	Al <sub>2</sub> O <sub>3</sub>	9.61	0.76
Cr <sub>2</sub> O <sub>3</sub>	—	—	Cr <sub>2</sub> O <sub>3</sub>	0.01	0.02
FeO	0.85	0.12	FeO	13.76	0.82
MnO	0.02	0.02	MnO	0.43	0.07
MgO	0.06	0.04	MgO	26.27	0.89
CaO	8.28	0.89	CaO	0.54	0.07
Na <sub>2</sub> O	5.18	0.25	Na <sub>2</sub> O	0.03	0.03
K <sub>2</sub> O	0.86	0.19	K <sub>2</sub> O	0.05	0.02
Total	99.97		Total	100.28	
Si (pfu)	10.521		Si (pfu)	1.752	
Al	5.468		Al IV	0.248	
Ti	0.007		Al VI	0.154	
Fe	0.128		Ti	0.007	
Mn	0.003		Cr	0.000	
Mg	0.017		Mg	1.391	
Ca	1.589		Fe	0.409	
Na	1.800		Mn	0.013	
K	0.197		Ca	0.020	
			Na	0.002	
			K	0.002	
Ab	50.26		Wo	1.11	
An	44.22		En	75.86	
Or	5.52		Fs	23.03	

sd = standard deviation (1 sigma). pfu = cations per formula unit on the basis of 32 and 6 oxygen for plagioclase and orthopyroxene, respectively.

Table 2. Chemical composition of glassy matrix from melt rock sample RK04/3 (mean of defocused beam electron microprobe analyses).

	n = 88	Sd	Max	Min
SiO <sub>2</sub> (wt%)	68.06	0.95	70.50	66.05
TiO <sub>2</sub>	0.35	0.07	0.54	0.22
Al <sub>2</sub> O <sub>3</sub>	15.42	0.66	17.09	13.67
FeO	1.82	0.49	3.42	0.93
MnO	0.06	0.03	0.16	<0.01
MgO	0.49	0.35	2.16	0.15
CaO	1.64	0.23	2.38	0.96
Na <sub>2</sub> O	2.73	0.27	3.26	2.05
K <sub>2</sub> O	5.15	0.46	5.88	4.10
Total	95.71	0.76	98.30	94.40

Sd = standard deviation (1 sigma).

rocks (e.g., metapelites or metagreywackes) also revealed orthopyroxenes of similar composition with high Al-contents (Skjerlie et al. 1993; Carrington and Harley 1995; Montel and Vielzeuf 1997). These high Al-orthopyroxenes are believed to represent metastable phases produced by disequilibrium conditions during fast cooling that inhibits Al-diffusion (Montel and Vielzeuf 1997 and references therein). Long orthopyroxene microlites are commonly fractured and displaced due to subsequent melt movement or shearing. Plagioclase microlites frequently crosscut fractured

orthopyroxenes, but the reverse has also been observed. Therefore, crystallization of orthopyroxene and plagioclase occurred almost simultaneously. Microlites also comprise euhedral titanomagnetite crystals of up to a few micrometers in width. The highly variable development of microlites and the presence of larger areas (several mm) of glass, some with perlitic cracks, indicates that the melts were rapidly quenched.

The sectioned samples all exhibit localized minor alteration, both in the matrices and in some clasts—particularly in feldspar or feldspar-bearing clasts. However, overall the samples are relatively fresh, especially considering the environment in which they were found (at the base of a sand dune where it is likely that moisture circulates). Also, the fact that significant amounts of volatiles were contained in the target material (and clast material, by implication, and on the basis of the high vesicle contents noted) allows for some alteration—and in this regard the material is rather of a relatively fresh appearance.

### Chemical Composition of Glass Matrix

Eighty-eight spot analyses of glass matrix in sample RK04/3 were carried out by electron microprobe. On average, the glass matrix is of granitic composition (Table 2).

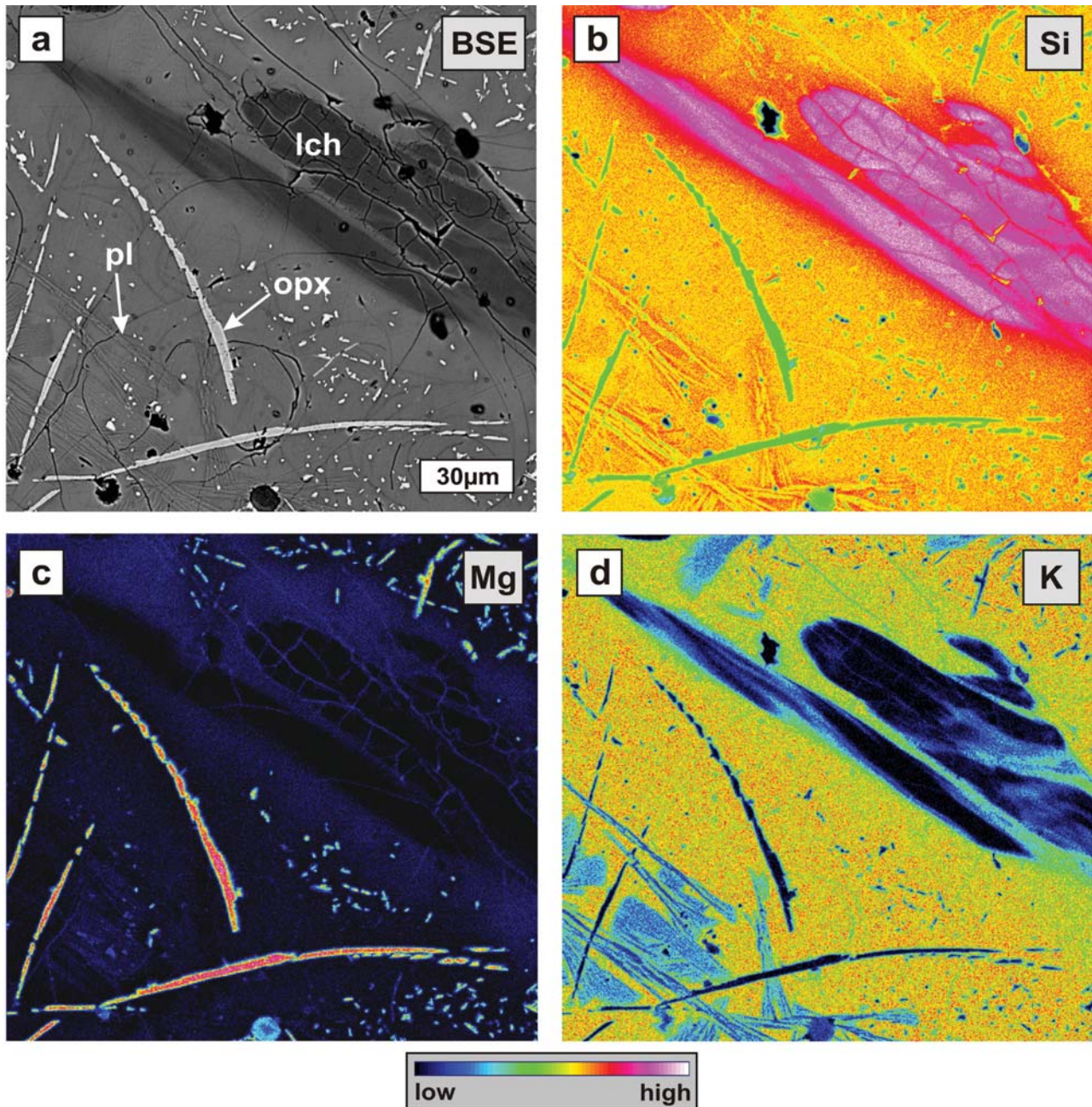


Fig. 3. Backscattered electron image (a) and corresponding mappings of relative element concentration (b, c, and d for Si, Mg, and K, respectively) performed with the electron microprobe. See color bar at the bottom of the figure for association of various colors to relative element concentration. The images show a typical section of the relatively clast poor sample RK04/3 with abundant plagioclase (pl) and orthopyroxene (opx) microphenocrysts within a glassy matrix. White spots in (a) represent titanomagnetite grains. Note the chemical heterogeneity of the glassy matrix in the vicinity of microphenocrysts and lechatelierite (lch).

The totals of the electron microprobe analyses are generally some weight percent below 100% which suggests some hydration of the glassy matrix. The chemical variation between single measurements indicates compositional heterogeneity of the glass matrix (Table 2, Figs. 3 and 4). This variation is largest for those elements that differ most in concentration between the glass matrix and the microlites of orthopyroxene, plagioclase, and titanomagnetite. The glass

matrix is the most important potassium-bearing phase of the melt rock with  $K_2O$  contents between about 4 and 6 wt% (Fig. 4). Element mapping indicates that the glass matrix is depleted in Mg, as well as Fe and Mn, within several micrometers to tens of micrometers wide haloes around orthopyroxene crystallites (Fig. 3). A halo of Si-enrichment occurs around plagioclase, lechatelierite, and quartz (Fig. 3b). Si-enrichment around plagioclase and Mg-, Fe-

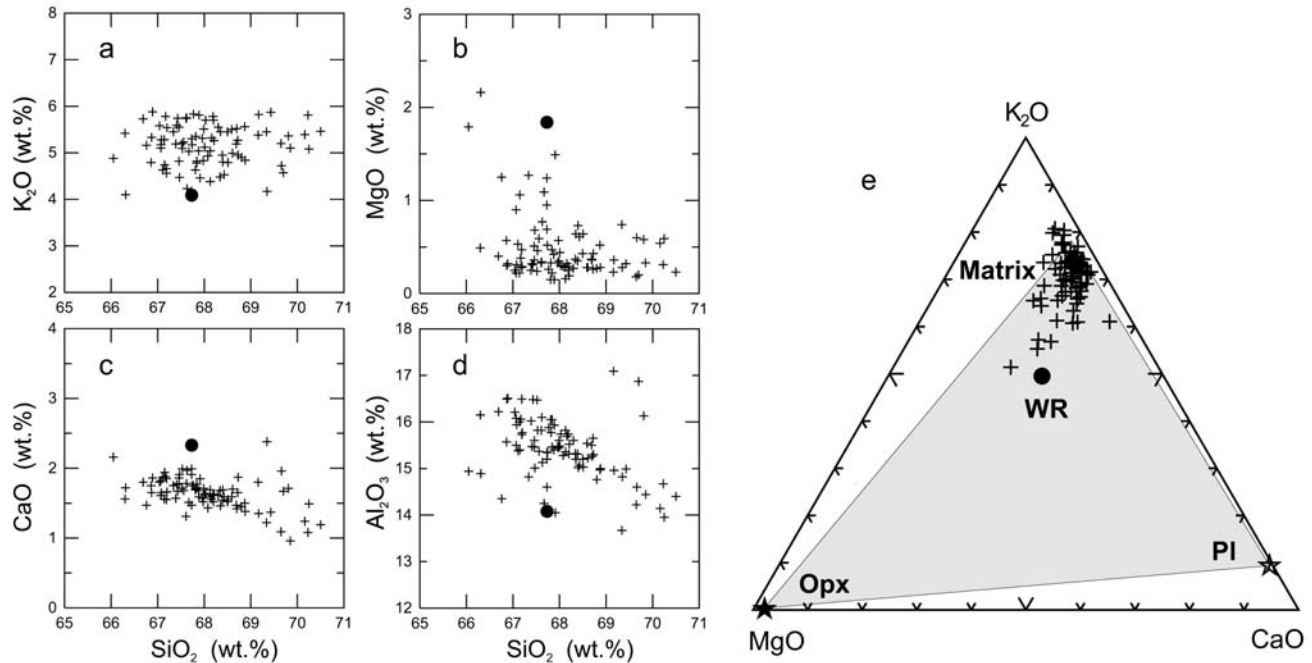


Fig. 4. a–d) Harker correlation diagrams of electron microprobe analyses of glassy matrix (crosses) in melt rock sample RK04/3 in comparison to the whole rock XRF analysis (solid circle, data from Table 3). e) Matrix analysis plotted in comparison to averages of the whole rock (WR), plagioclase (pl) and orthopyroxene (opx) composition of sample RK04/3.

and Mn-depletion around orthopyroxene is most likely due to fractionation of those elements into the two liquidus phases during rapid crystallization. Si-enrichment around lechatelierite and quartz is due to partial dissolution of these phases in the melt (Fig. 3b). Enhanced melt viscosity during rapid cooling inhibited element diffusion and, thus, complete homogenization of the melt matrix during and after microlite crystallization.

### Whole-Rock Chemical Compositions

#### Major and Trace Element Contents

Chemical analysis of the five whole-rock samples shows that the melt rock body is homogeneous for most major and trace elements (Table 3, Fig. 5), at least at the sub-sample level (several cm<sup>3</sup>). In those cases where data from several analytical methods are available for one element, only the value of the method is listed that has the highest precision and lowest detection limits, e.g., ICP-MS data for Co, Ni, and Cr instead of XRF data. The melt rock samples of RK04 and URK41 and the average suevite samples are of broadly granitic to granodioritic composition (Table 3), and similar to the upper continental crust (see Taylor and McLennan 1985, 1995). The acidic to intermediate orthogneisses of the target area are most likely the dominant precursor lithology for the Roter Kamm melt rock and suevite (Fig. 5), as also suggested by Reimold and Miller (1989) and Reimold et al. (1994). Higher Fe<sub>2</sub>O<sub>3</sub>, MgO, and lower SiO<sub>2</sub> contents of the only previously analyzed melt rock sample URK41 (Reimold and

Miller 1989) in comparison to the RK04 melt rock and average suevite samples suggests that more mafic rocks were involved in the formation of the URK41 melt rock. This mafic rock component is represented by basic orthogneisses and biotite-hornblende clasts (samples 1, 101, and 86 C; Reimold and Miller 1989). These basic to ultrabasic rocks have lower light rare earth element to heavy rare earth element (LREE/HREE) ratios and may also show higher middle rare earth element (MREE) and HREE contents compared to the acid to intermediate orthogneisses (Fig. 6). Therefore, the mixing between these MREE- and HREE-rich basic gneisses with the acidic and intermediate orthogneisses could also explain the enhanced MREE and HREE content of URK41 melt rock compared to the RK04 melt rock and the average suevite (Fig. 6). The Ni, Cr, and Co values of the Roter Kamm melt rock (Table 3) are also close to the values for upper continental crust (Cr = 35 ppm, Ni = 19 ppm, and Co = 12 ppm, after Wedepohl 1995, or Cr = 85 ppm, Ni = 44 ppm, and Co = 17 ppm, after Taylor and McLennan 1985). The Ir value of 0.24 ppb for the bulk melt rock is certainly elevated compared to average crustal abundances (about 0.02 ppb; Taylor and McLennan 1985) and compared to the contents of the various target rocks (e.g., Reimold et al. 1994).

#### Platinum Group Elements (PGE)

Enrichments in the PGE abundances and PGE interelement abundance ratios can provide evidence for a meteoritic component in impactites and even help to identify the impactor type (see review by Koeberl 1998). In

Table 3. Chemical composition of impact-melt rock and suevite from Roter Kamm.

		RK04 3-1	RK04 3-2	RK04 3-3	RK04 5	RK04 6	Average RK04	URK41	Average Suevite <sup>1</sup>
	Meth	Melt rock	Melt rock	Melt rock	Melt rock	Melt rock	Melt rock	Melt rock	
SiO <sub>2</sub> wt%	(1)	68.5	68.2	67.0	67.4	67.9	67.8	65.5	67.0
TiO <sub>2</sub>	(1)	0.41	0.40	0.39	0.38	0.38	0.39	0.40	0.31
Al <sub>2</sub> O <sub>3</sub>	(1)	13.76	13.69	13.80	14.50	14.00	13.95	14.30	13.42
Fe <sub>2</sub> O <sub>3</sub>	(1)	4.01	3.90	3.67	3.64	3.54	3.75	6.40	3.88
MnO	(1)	0.09	0.09	0.09	0.08	0.08	0.09	0.10	0.08
MgO	(1)	1.84	1.85	1.86	1.83	1.83	1.84	3.00	3.14
CaO	(1)	2.40	2.26	2.33	2.25	2.41	2.33	2.00	1.97
Na <sub>2</sub> O	(1)	2.55	2.56	2.62	2.71	2.50	2.59	1.60	1.94
K <sub>2</sub> O	(1)	4.02	4.04	4.45	3.99	4.10	4.12	4.20	4.08
P <sub>2</sub> O <sub>5</sub>	(1)	0.14	0.14	0.12	0.13	0.13	0.13	0.50	0.14
LOI	(1)	2.75	2.77	2.90	2.70	2.40	2.70	1.80	3.59
Total		100.44	99.90	99.23	99.61	99.27	99.69	99.80	99.55
Sc ppm	(2)	–	8.6	–	–	–	8.6	12.2	10.9
V	(1)	70	66	71	62	67	67	–	101
Cr	(4)	36.7	28.1 <sup>(2)</sup>	20.8	23.6	24.8	26	65	52
Co	(4)	10.9	8.4 <sup>(2)</sup>	8.5	10.9	10.0	10.1	17.8	14.6
Ni	(4)	32	25 <sup>(1)</sup>	18.3	22.4	23.1	24.0	28	32.8
Cu	(1)	30	29	<30	<30	<30	30	–	30
Zn	(1)	47	45	48	51	46	47	–	61
As	(2)	–	0.1	–	–	–	0.1	–	1.1
Se	(2)	–	0.2	–	–	–	0.2	–	0.3
Br	(2)	–	0.1	–	–	–	0.1	–	0.1
Rb	(1)	178	176	207	181	183	185	221	189
Sr	(1)	210	206	212	236	223	217	–	295
Y	(1)	33	33	54	49	46	43	–	17
Zr	(1)	136	137	175	154	151	151	–	140
Nb	(1)	17	17	<10	<10	<10	17	–	11
Sb	(2)	–	0.09	–	–	–	0.09	0.09	0.34
Cs	(2)	–	4.0	–	–	–	4.0	7.0	4.1
Ba	(1)	1488	1440	1340	1377	1385	1406	1725	1758
La	(2)	–	30.2	–	–	–	30.2	49.0	41.9
Ce	(2)	–	61.3	–	–	–	61.3	59.0	80.3
Nd	(2)	–	29.1	–	–	–	29.1	28.0	36.9
Sm	(2)	–	4.67	–	–	–	4.67	6.70	4.77
Eu	(2)	–	0.89	–	–	–	0.89	1.20	0.97
Gd	(2)	–	4.90	–	–	–	4.90	–	3.88
Tb	(2)	–	0.77	–	–	–	0.77	1.50	0.55
Tm	(2)	–	0.44	–	–	–	0.44	–	0.28
Yb	(2)	–	2.92	–	–	–	2.92	1.11	1.60
Lu	(2)	–	0.45	–	–	–	0.45	0.50	0.23
Hf	(2)	–	3.66	–	–	–	3.66	2.50	3.96
Ta	(2)	–	0.88	–	–	–	0.88	0.78	0.87
Ir (ppb)	(3)	–	0.24	–	–	–	0.24	–	–
Au (ppb)	(2)	–	0.8	–	–	–	0.8	6.0	2.8
Th	(2)	–	24.5	26.0	25.0	24.0	24.9	12.2	39.8
U	(2)	–	4.0	<10	<10	<10	4.0	4.2	3.3

Meth = analytical method, (1) = XRF, (2) = INAA, (3) = INAA with gamma-gamma multi-parameter spectrometry, (4) = ICP-MS.

<sup>1</sup>After Reimold et al. (1997), URK41 after Reimold and Miller (1989).

total, 12 PGE analyses have been obtained from 6 melt rock samples, including the INAA value of 0.24 ppb for Ir in the bulk rock (Tables 3 and 4). With the exception of two samples, the PGE concentrations of most aliquots are relatively low. In contrast to Cr, Ni and Co values, however, the PGE are enriched compared to the most common rocks

of the Earth's crust or mantle (Fig. 7, Table 5). Although the Cr values show little variation, Ir varies by one order of magnitude with  $I_{r_{max}} = 0.87$  ppm. The rather large variation of PGE contents between samples or sample aliquots that are generally very homogeneous with respect to most major and trace elements indicate significantly heterogeneous

Table 4. Whole rock abundances of the platinum group elements in several aliquots of Roter Kamm melt rock samples from locality RK04, determined by ICP-MS.

Sample	Ir (ng/g)	Ru (ng/g)	Pt (ng/g)	Rh (ng/g)	Pd (ng/g)	Au (ng/g)	Sample mass (g)
RK 04/3-1	0.87	0.92	2.34	0.35	2.01	0.56	25
RK 04/3-2	0.54	0.95	1.90	0.34	1.45	0.43	13
RK 04/3-3 a	0.06	0.18	0.49	0.06	0.75	0.23	50
RK 04/3-3 b	0.18	0.32	0.69	0.10	0.83	0.25	39
RK 04/3-3 c	0.07	0.15	0.49	0.07	0.74	b.l.d.	34
RK 04/3-3 d	0.08	0.16	0.42	0.06	0.60	b.l.d.	25
RK 04/3-3 e	b.l.d.	0.06	0.43	0.05	0.67	b.l.d.	38
RK 04/3-3 avg.	0.10	0.17	0.50	0.07	0.72	0.24	
RK 04/5 a	0.09	0.24	0.74	0.09	0.79	0.19	51
RK 04/5 b	0.07	0.18	0.71	0.07	0.86	0.26	60
RK 04/5 avg.	0.08	0.21	0.73	0.08	0.82	0.22	
RK 04/6 a	0.20	0.32	0.88	0.12	0.95	0.19	35
RK 04/6 b	0.17	0.27	0.74	0.10	0.79	0.17	59
RK 04/6 avg.	0.18	0.29	0.81	0.11	0.87	0.18	
l.d.	0.06	0.06	0.1	0.01	0.14	0.13	
error $\pm$	0.01	0.05	0.05	0.01	0.08	0.02	
Continental crust	0.02	0.21	0.51	0.06	0.52	2.50	

l.d. = limit of detection (see Tagle and Claeys 2005); b.l.d. = below limit of detection. Values for the continental crust from Peucker-Ehrenbrink and Jahn (2001), Rh value from Wedepohl (1995).

distribution of the PGE. There is a positive correlation of Ir with Cr following a mixing line that is typical for mixing of crustal terrestrial rocks with chondritic projectiles (Fig. 7, Tagle and Hecht 2006).

The CI-normalized PGE patterns for the Roter Kamm impact melt are in all samples similar to that of continental crust, with the main exception being the relative enrichment of Ir (Fig. 8). The relatively flat patterns suggest that the projectile could have been chondritic. In order to exclude the effect of the indigenous component, which is most likely relatively small, but nevertheless overlaps the projectile signature, we have calculated the projectile elemental ratios following the procedure described in detail by Tagle and Hecht (2006). The projectile elemental ratios determined by calculating the slope of the mixing line between target and projectile values is mainly controlled by the element ratios of the latter, which allows to determine the element ratios for the projectile without taking the indigenous component into consideration. Figure 9 shows plots of various PGE ratios for the Roter Kamm impact-melt sample aliquots. The parameters of the linear regression are included in each diagram together with the ranges of the respective element ratios for different types of chondrites. The PGE ratio correlations are relatively good. However, the two samples with the highest concentrations have a strong influence on the slope, and some elements in these two samples give ratios that do not fit into the correlation (see Fig. 9, Ru/Ir and Rh/Ir correlation). Mainly because of the small number of individual samples available, and the fact that only two aliquots showed a significant projectile component, it is

impossible to make a final assessment of the projectile type. However, the projectile elemental ratios are for almost all element combinations within the range of chondrites. If we take Rh/Ir and Pd/Ir ratios at face value for the projectile elemental ratios, it is possible to exclude a carbonaceous chondrite projectile, as only the element ratios of enstatite and ordinary chondrites are higher than 0.30 for Rh/Ir and 1.2 for Pd/Ir, compared to the ratios found in Roter Kamm (0.35 and 1.4, respectively) (ratios for chondrites according to McDonald et al. 2001 and Tagle and Berlin 2008). Furthermore, the overall chondritic PGE ratios at the Roter Kamm melt rock excludes an iron projectiles which are characterized by highly fractionated PGE pattern. The proportion of projectile is extremely small (roughly between 0.01 and 0.2%, Fig. 7), which does not support the use of Cr-isotopes for projectile identification in the case of Roter Kamm (cf. Koeberl et al. 2007).

#### <sup>40</sup>Ar/<sup>39</sup>Ar Dating

Sample RK 04/03 was selected for <sup>40</sup>Ar/<sup>39</sup>Ar laser probe dating because most sections showed relatively low density of clasts and predominance of tiny quartz clasts. Most relatively sizable clasts (<300  $\mu$ m) are also completely annealed. However, on the bulk of these observations it can not be excluded that this sample could also have contained some areas that were more clast rich. Neither of the two sub-samples (RK04-03A, RK04-03B) yielded plateau ages. RK04-03A gave a discordant spectrum comprising 8 steps (Fig. 10a) and sample RK04-03B comprises 12 steps, is

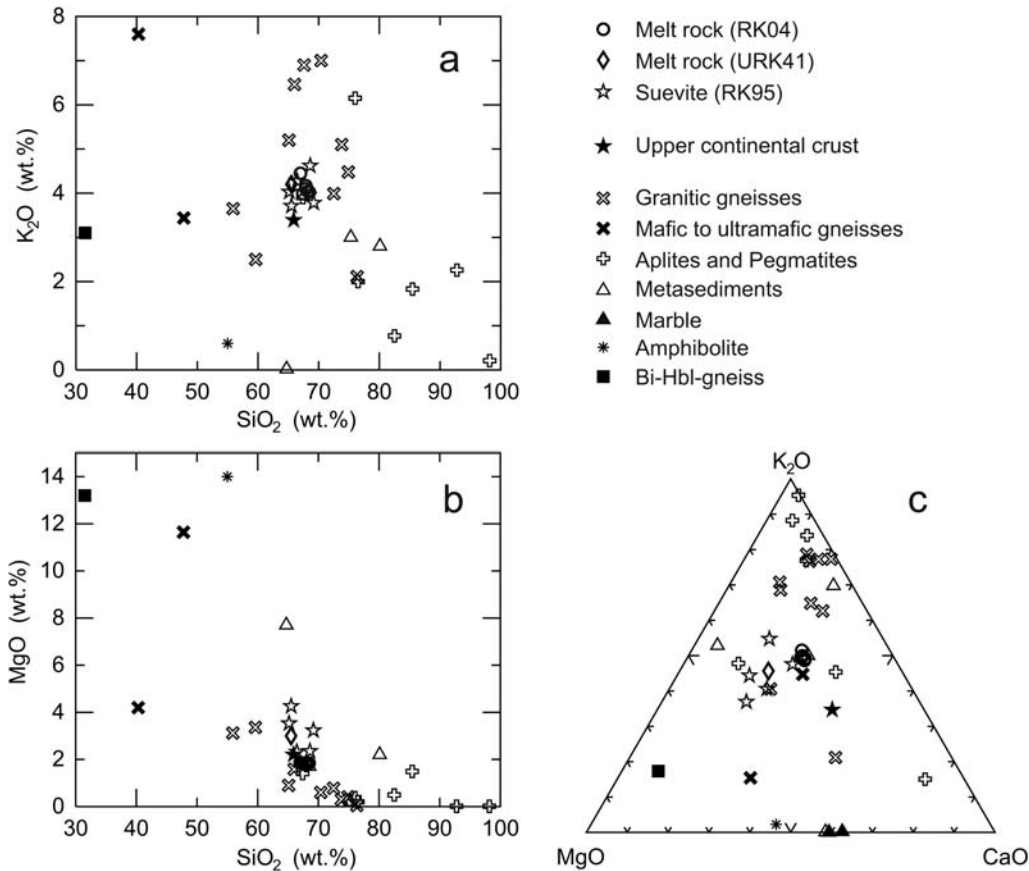


Fig. 5. Harker correlation diagrams (a, b) and triangular plot (c) of the chemical composition of melt rock samples from RK04 in comparison to suevite, melt rock sample URK41, and country rocks from Roter Kamm (data from Reimold and Miller 1989; Reimold et al. 1994, 1997). Composition of the continental crust after Taylor and McLennan (1985).

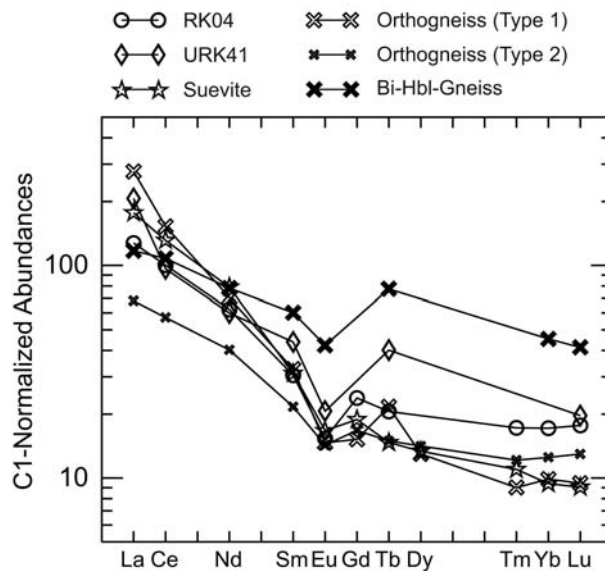


Fig. 6. Chondrite-normalized rare earth element patterns of Roter Kamm melt rocks (RK04 and URK41) in comparison to the respective patterns of average suevite and average acid to ultrabasic basement gneisses. Orthogneiss of type 1 (average of granitic samples 8, 17, 18, 85, 88, 89, 31-B, and 39), Orthogneiss of type 2 (average of basic to intermediate gneisses 108, 109, 110), Bio-Hbl gneiss = biotite-hornblende gneiss (average of samples 1, 86C). Except for the melt-rock sample RK04/3 (this study), the data are from Reimold and Miller (1989) and Reimold et al. (1994, 1997).

Table 5.  $^{40}\text{Ar}$ - $^{39}\text{Ar}$  analytical data of two aliquots from melt-rock sample RK04/3.

Sample	Step no.	$^{40}\text{Ar}$	$\pm$	$^{39}\text{Ar}$	$\pm$	$^{38}\text{Ar}$	$\pm$	$^{37}\text{Ar}$	$\pm$	$^{36}\text{Ar}$	$\pm$	$^{40}\text{Ar}^*/^{39}\text{Ar}$	$\pm$	Age (Ma)	$\pm$
RK04/3A	1	0.4327	0.0045	0.0169	0.0000	0.0007	0.0001	0.1114	0.0200	0.0005	0.0000	16.1308	0.3735	3.8954	0.1843
RK04/3A	2	0.8369	0.0022	0.0332	0.0001	0.0008	0.0000	0.0700	0.0042	0.0005	0.0001	20.6744	0.4517	4.9911	0.2234
RK04/3A	3	1.1919	0.0019	0.0468	0.0001	0.0011	0.0000	0.0807	0.0047	0.0010	0.0001	19.4252	0.3604	4.6899	0.1800
RK04/3A	4	4.5282	0.0011	0.0284	0.0000	0.0038	0.0000	0.2698	0.0047	0.0132	0.0000	22.5612	0.2375	5.4459	0.1267
RK04/3A	5	1.0666	0.0010	0.0296	0.0000	0.0009	0.0000	0.0617	0.0047	0.0017	0.0000	19.4168	0.4140	4.6879	0.2051
RK04/3A	6	0.6217	0.0017	0.0200	0.0001	0.0005	0.0000	0.0575	0.0087	0.0009	0.0001	17.8364	0.7593	4.3068	0.3687
RK04/3A	7	0.3759	0.0005	0.0110	0.0000	0.0003	0.0000	0.0086	0.0048	0.0005	0.0000	20.7494	0.8187	5.0092	0.3979
RK04/3A	8	0.0286	0.0002	0.0008	0.0000	0.0001	0.0000	0.0151	0.0048	0.0001	0.0000	8.0864	4.4091	1.9538	2.1295
RK04/3B	1	0.1463	0.0002	0.0005	0.0000	0.0001	0.0000	0.0184	0.0119	0.0001	0.0000	237.5849	19.4801	56.5407	9.1448
RK04/3B	2	0.0591	0.0001	0.0011	0.0000	0.0001	0.0000	0.0162	0.0119	0.0001	0.0000	35.1381	7.1446	8.4747	3.4392
RK04/3B	3	0.0545	0.0001	0.0012	0.0000	0.0001	0.0000	0.0130	0.0088	0.0001	0.0000	30.8227	9.7884	7.4360	4.7137
RK04/3B	4	0.2545	0.0005	0.0080	0.0000	0.0002	0.0000	0.0325	0.0088	0.0003	0.0000	20.6407	1.7072	4.9830	0.8247
RK04/3B	5	1.8573	0.0039	0.0576	0.0001	0.0014	0.0001	0.0792	0.0196	0.0023	0.0001	20.2375	0.5224	4.8858	0.2566
RK04/3B	6	0.3625	0.0011	0.0119	0.0000	0.0003	0.0001	0.0528	0.0197	0.0004	0.0000	20.6328	1.1591	4.9811	0.5611
RK04/3B	7	0.6226	0.0003	0.0157	0.0000	0.0004	0.0000	0.0264	0.0111	0.0007	0.0000	26.2633	0.6372	6.3380	0.3135
RK04/3B	8	0.4677	0.0012	0.0149	0.0000	0.0005	0.0000	0.0353	0.0111	0.0006	0.0000	19.6230	0.3717	4.7376	0.1854
RK04/3B	9	0.3268	0.0006	0.0106	0.0000	0.0002	0.0000	0.0298	0.0143	0.0003	0.0000	22.0772	1.0131	5.3293	0.4913
RK04/3B	10	0.3966	0.0007	0.0125	0.0000	0.0003	0.0000	0.0408	0.0143	0.0005	0.0000	20.3609	0.8592	4.9155	0.4172
RK04/3B	11	0.2827	0.0004	0.0072	0.0001	0.0002	0.0001	0.0221	0.0154	0.0003	0.0001	26.0998	2.3043	6.2986	1.1120
RK04/3B	12	0.0941	0.0002	0.0025	0.0001	0.0001	0.0001	0.0221	0.0154	0.0002	0.0001	15.5520	6.7449	3.7558	3.2546

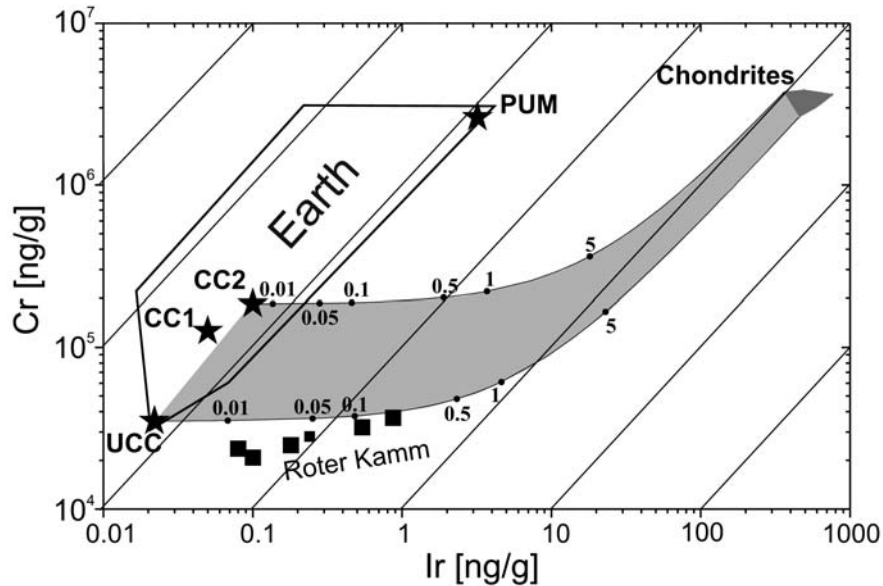


Fig. 7. Plot of Cr versus Ir concentrations in terrestrial target rocks compared to the composition of impact-melt rock samples from Roter Kamm (large squares = ICP-MS, small square = INAA). The gray field indicates the most likely mixing lines between chondritic projectiles and common terrestrial targets. Numbers above and below the grey field represent wt% chondritic material in the mixing lines. Numbers above and right of the diagram provide the values for the constant ratios represented by the lines crossing the log-log plot. UCC = upper continental crust (Wedepohl 1995), CC1 = total continental crust (Wedepohl 1995), CC2 = total continental crust (Taylor and McLennan 1985), PUM = primitive upper mantle (McDonough and Sun 1995). A detailed description of the composition data for terrestrial rocks used for this plot is given in a compilation of literature data by Tagle and Hecht (2006).

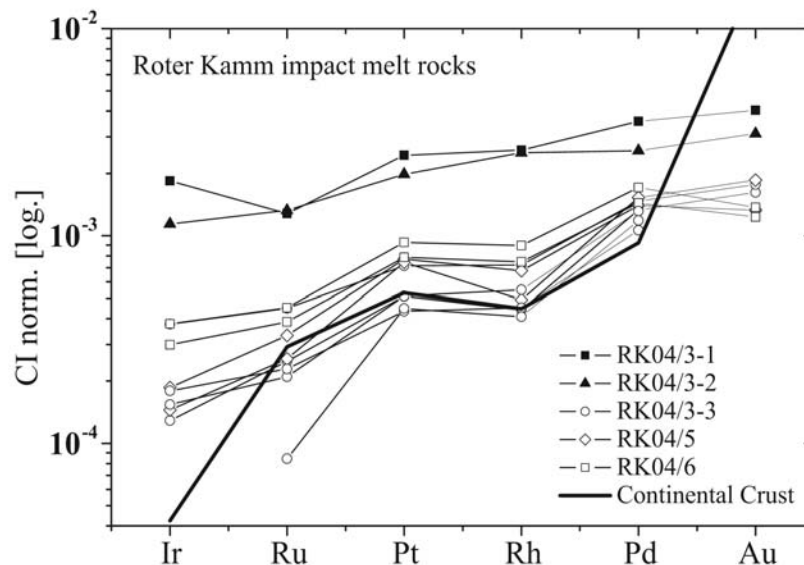


Fig. 8. Abundances of the PGEs and Au normalized to carbonaceous chondritic (CI) concentrations in the impact-melt rock samples from Roter Kamm, compared to the composition of the average continental crust. For source of data see Table 4.

also discordant (Fig. 10b). Individual ages obtained vary between 3.9 and 6.3 Ma (Table 5). Both samples have variable atmospheric argon components. For sample RK04-03A it ranges from 14% to 81%, for sample RK04-03B from 41% to 87%. This becomes important when plotting the data on an inverse isochron correlation diagram; for sample RK04-03A the data are widely spread and the line of best fit intercepts

within error of the  $^{36}\text{Ar}/^{40}\text{Ar}$  value for air (0.00338), with an intercept age of  $4.69 \pm 0.31$  Ma (Fig. 10e). For sample RK04-03B the majority of the data are grouped, with relatively high  $^{39}\text{Ar}/^{40}\text{Ar}$  values ( $\sim 0.035$ ) but low  $^{36}\text{Ar}/^{40}\text{Ar}$  values ( $\sim 0.001$ ) (Fig. 10f). Three data points have lower  $^{39}\text{Ar}/^{40}\text{Ar}$  values ( $< 0.027$ ) with large uncertainties on the  $^{36}\text{Ar}/^{40}\text{Ar}$  ratios (Fig. 10f); these indicate the likely presence

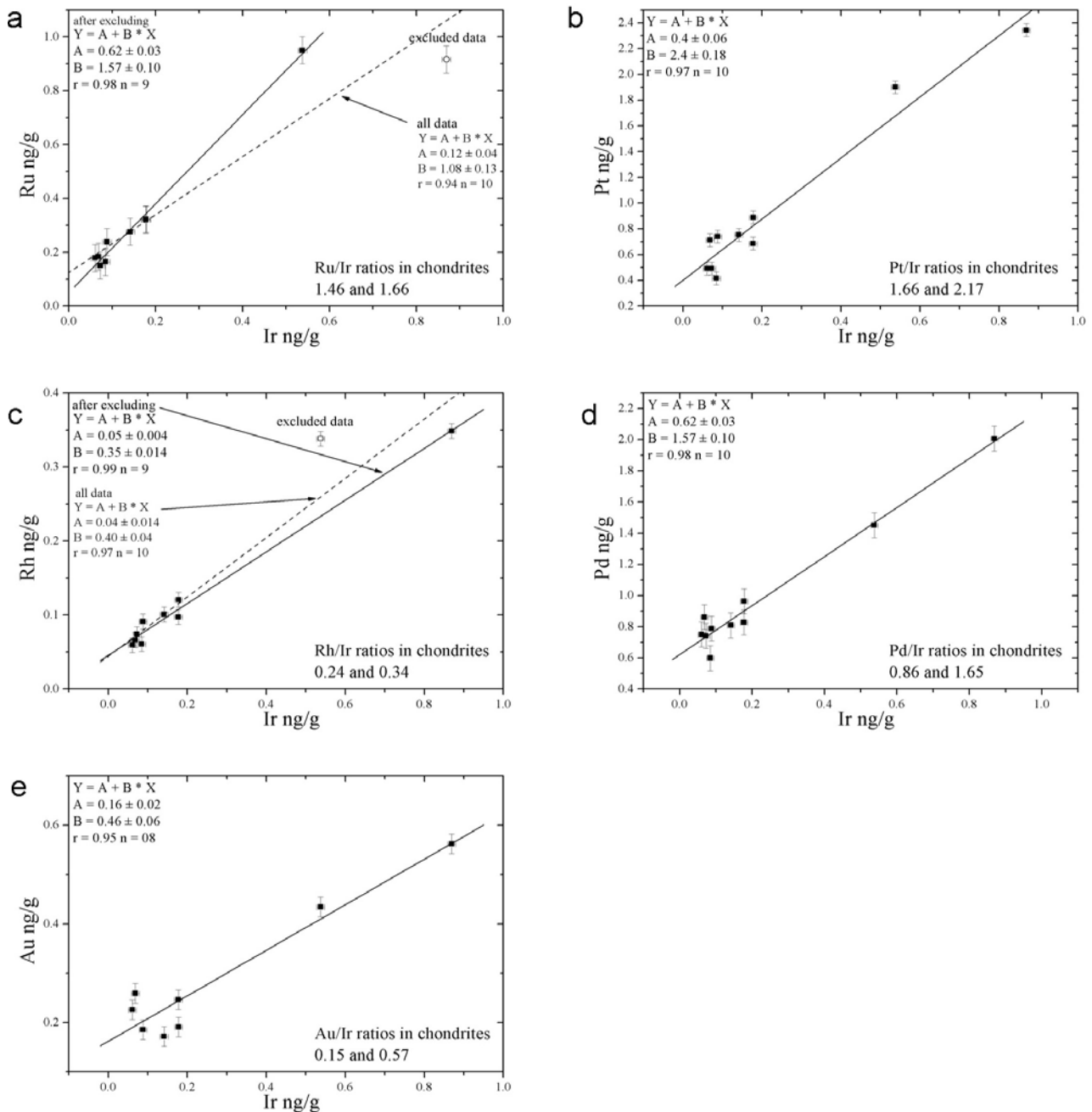


Fig. 9. Linear regression analysis of PGE (a–d) and Au (e) versus Ir of Roter Kamm melt rock samples (see Table 4). The slopes of the mixing lines (B) represent the ratios in the projectile. The range of the respective ratios within different chondrite groups (data from Tagle and Berlin 2008) are given in the lower right corner of each diagram.

of a small quantity of excess  $^{40}\text{Ar}$  in this sample. For this sample, if a regression is forced through the value for air, the intercept age is  $5.06 \pm 0.44$  Ma (Fig. 10f).

## DISCUSSION AND CONCLUSIONS

We report on the finding of a massive impact-melt rock occurrence (at least  $2 \times 1$  m) at the top of the southwestern part of the rim of the Roter Kamm crater. It does remain

uncertain whether this material was emplaced ballistically or as part of a melt flow from the crater interior.

## Shock Metamorphism and Melt Rock Composition

The range of shock deformation textures observed indicates that most of the clast material is either unshocked or did not exceed a shock metamorphic grade of 10–15 GPa (rare PDFs formed); this material accounts for roughly 70%

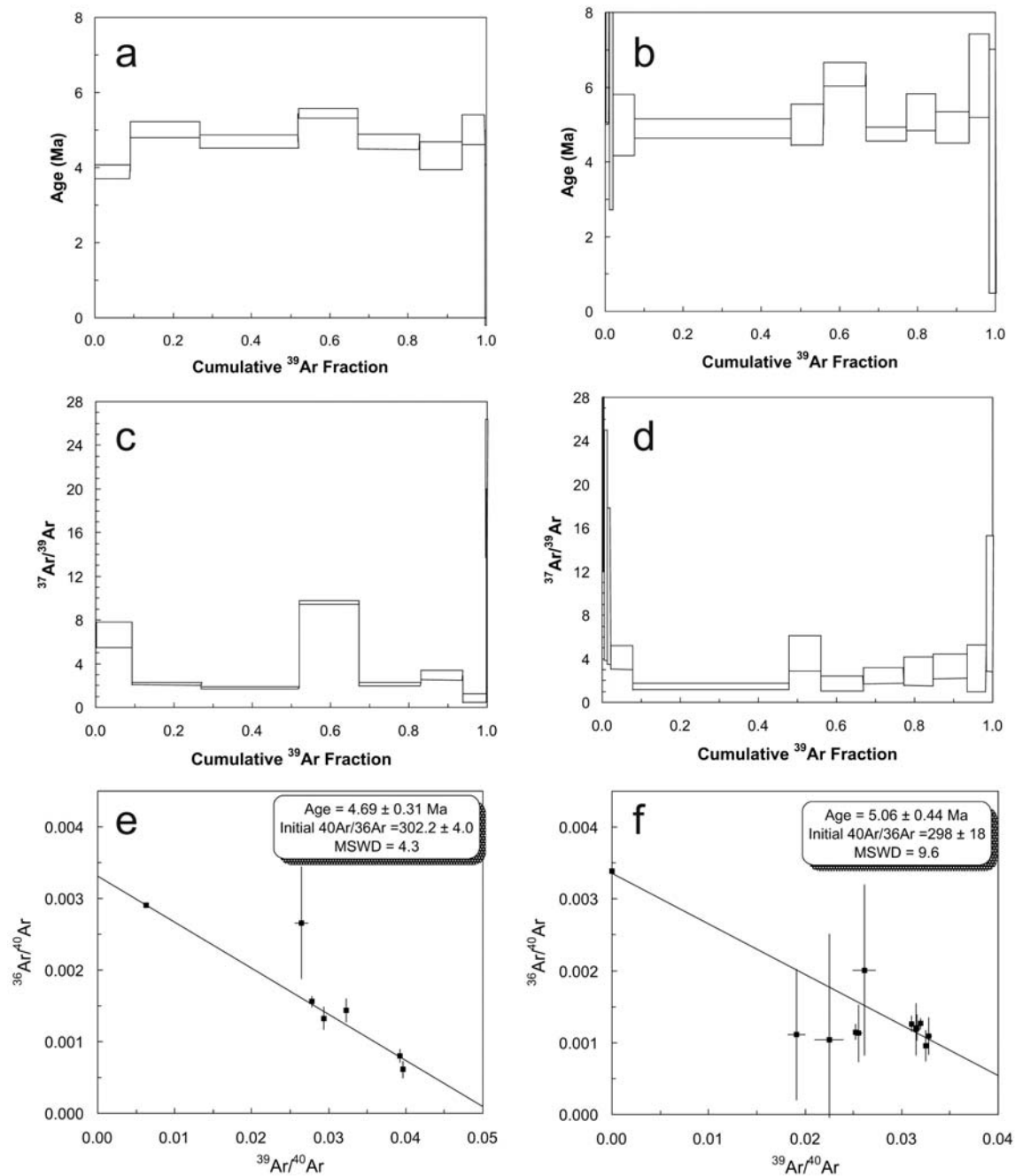


Fig. 10.  $^{40}\text{Ar}$ - $^{39}\text{Ar}$  age spectrum diagrams. a) RK04/3A step-heating spectrum. b) RK04/3B step-heating spectrum. c) Sample RK04/3A:  $^{37}\text{Ar}/^{39}\text{Ar}$  versus  $^{39}\text{Ar}$  release. d) Sample RK04/3B  $^{37}\text{Ar}/^{39}\text{Ar}$  versus  $^{39}\text{Ar}$  release. e) RK04/3A inverse isochron correlation diagram. f) RK04/3B inverse isochron correlation diagram.

of the overall clast content. The shock range between 10–15 and 30 GPa (up to the onset of formation of diaplectic glass) is poorly represented (estimated at <5% of clast load). The remaining ca. 25% clastic material are highly shocked, with diaplectic glass formation and partial or complete melting (feldspar melts and lechatelierite). On the other hand, the melt groundmass relates to bulk melting of target rock, which would have required shock pressures in excess of 45 GPa. This broad pattern of shock effects, with essentially very little

or even lack of effects of moderate shock degree (rarity or lack of PDFs), has been observed for melt rock samples from a range of impact structures at all scales. One example is the fact that Vredefort Granophyre contains only a tiny amount of shocked (i.e., non-melted or non-diaplectic) clasts (Buchanan and Reimold 2002).

The clast content provides information on the composition of the target rock that melted, even though there are limits to this approach due to preferential melting of

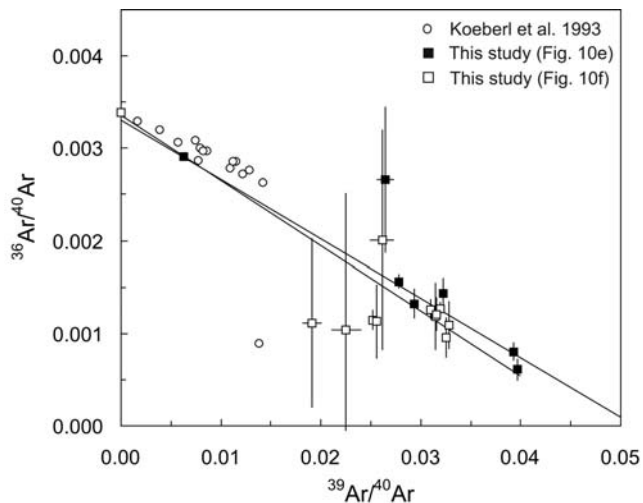


Fig. 11. Inverse isochron correlation diagram comparing the new data for samples RK04/03 A and B and the results of Koeberl et al. (1993).

volatile-enriched materials. Granitic clasts—i.e., those composed of quartz, feldspar and biotite mineral aggregates—are rare but notable. Quartz and feldspar could be derived from granitic precursor rock, vein quartz which is a prominent component of the pre-impact target (Reimold and Miller 1989; Reimold et al. 1994), or sedimentary sources. However the rarity of sandstone or quartzitic clasts suggests that the more important component was granitic basement. Some dense, black, seemingly oxidized patches up to several mm long, in places have relics of a banding, which is tentatively interpreted as sedimentary layering, and so this material is considered to be mica schist/shale of the type discussed by Reimold and Miller (1989) and Degenhardt et al. (1996). All of the analyzed samples from the same outcrop are chemically rather similar, indicating mixing of the melt at least at the meter-scale, represented by this new exposure. In comparison to URK41, however, distinct differences such as lower Fe and Mg, and higher Si are noted. Major and trace element composition of both melt rocks suggest their formation from predominantly granitoid basement, whereby the new sample suite provides evidence for a comparatively somewhat reduced contribution from more mafic components, as, for example, demonstrated by the respective REE patterns (cf. Fig. 6). Incomplete digestion of target rock fragments is indicated by textural and micro-chemical observations. In addition we note incomplete chemical mixing of melts and chemical disequilibrium due to rapid cooling and crystallization, indicated by schlieren textures and element mapping results.

### Impactor Characterization

The elevated abundances of Ir and other siderophile elements compared to the target rocks and the average

continental crust provide—for the first time at Roter Kamm—a clear indication of the presence of an extraterrestrial component in the melt rock. However, melt rock heterogeneity caused by incomplete melting of the target, or incomplete mixing of melts from different target rocks or target rock components, may have consequences for the chemical identification of the projectile or radiometric age dating. With a low degree of impactor contamination, a precise identification of the projectile via PGE-ratios following Tagle and Hecht (2006) requires a high degree of target rock homogenization during impact melt formation. This is important because several impact-melt samples of similar indigenous PGE contents, but various degree of impactor contamination, are required for calculation of the mixing line that then may characterizes the PGE-ratio of the projectile and, where possible, a certain chondrite type (see, e.g., McDonald et al. 2001; McDonald 2002; Tagle and Hecht 2006). Nevertheless, based on both PGE patterns and ratio plots for the analyzed Roter Kamm melt rock samples (Figs. 8 and 9) the projectile responsible for the formation of the Roter Kamm impact structure was most likely a chondrite of a non-carbonaceous type. Roter Kamm represents so far the smallest crater ever identified as produced by the impact of a chondritic projectile (except the Carancas meteorite crater of 14 m diameter, formed on the 15th of September 2007 in Peru; Kenkmann et al. 2008), which is about one kilometer smaller than the New Quebec crater of 3.4 km in diameter (Grieve et al. 1991).

### Roter Kamm Impact Age

Both samples investigated by  $^{40}\text{Ar}/^{39}\text{Ar}$  laser probe dating yield discordant step-heating spectra; the two corresponding intercept ages ( $4.69 \pm 0.31$  and  $5.06 \pm 0.44$  Ma) are within error of one another. Although there is possibly a minor component of excess  $^{40}\text{Ar}$  in RK04-03B, these intercept ages could represent an approximation of the maximum age for the Roter Kamm impact. The best age derived from these experiments for Roter Kamm is calculated by taking a weighted mean of the two intercept ages, and is  $4.81 \pm 0.5$  Ma (MSWD = 0.47).

Clearly these ages confirm a relatively young age for this impact event, as previously indicated by Koeberl et al. (1993) based on a single  $^{40}\text{Ar}/^{39}\text{Ar}$  step-heating experiment performed on melt breccia sample URK41. Their age of  $3.7 \pm 0.3$  Ma is clearly different from the new results outside of error limits, but our new data indicate that the real age of this impact event should be of the order of 4–5 Ma. The data in Koeberl et al. (1993) were derived from a total gas age of a large sample of URK41 glass (175.9 mg, compared with our ca. 10 mg sample) and a smaller aliquot of the same sample but a different colored glass. Neither of these two samples yielded statistically valid plateau ages, although Table 3b in Koeberl et al. (1993) describes a plateau age of  $4.30 \pm 0.28$  Ma

for sample URK41 light glass. The preferred age of Koeberl et al. (1993) is  $3.7 \pm 0.3$  Ma, based on the minimum age of 3.6 from the URK41 light glass, and the total gas age of  $3.7 \pm 0.3$  Ma from URK41 dark glass, younger than our age of  $4.81 \pm 0.5$  Ma. Plotting the data of Koeberl et al. (1993) with our new data on an inverse isochron correlation diagram (Fig. 11) it becomes apparent that there are significant differences in the radiogenic and atmospheric argon contents. The previously published data have very low levels of radiogenic argon and concomitant high atmospheric argon components (Fig. 11), indicating a high degree of alteration in the glass. Given that our sample contains significantly more radiogenic argon we believe that our data are more robust. Figure 11 highlights the difficulty in obtaining consistent age data from impact-melt rocks.

After the recently-reported age complexities for the Siljan (Reimold et al. 2005), Haughton (Sherlock et al. 2005) and Jänisjärvi (Jourdan et al. 2007c) impacts, whereby the previously accepted ages, in all these cases judged as well-constrained, had to be revised by significant amounts (millions to tens of millions of years), Roter Kamm is another case where a seemingly good age has become less robust through renewed  $^{40}\text{Ar}/^{39}\text{Ar}$  dating. This suggests that there may be further flaws in the already less than sufficient statistics of terrestrial impact ages (Jourdan et al. 2007b; Reimold 2007; Kelley 2007) and highlights the need for ongoing high-resolution chronology of impact-melt rocks, including further chronological effort on Roter Kamm impact-melt rocks.

*Acknowledgments*—We thank Peter Czaja, Katrin Krahn, and Hans-Rudolf Knöfler for technical lab support. This work was supported by the Austrian FWF (grant P18862-N10, to C. K.) and the Deutsche Akademie der Naturforscher Leopoldina (grant BMBF-LPD 9901/8-130 to R. T.). S. C. S. acknowledges support from NERC (NER/I/S/2002/00692). We appreciate the comments by reviewers D. Bogard and D. Rajmon, as well as the suggestions by associate editor J. G. Spray.

*Editorial Handling*—Dr. John Spray

## REFERENCES

- Brandt D., Reimold W. U., Franzen A. J., Koeberl C., and Wendorff L. 1998. The geophysical signature of the Roter Kamm impact crater, Namibia. *Meteoritics & Planetary Science* 33:447–454.
- Carrington D. P. and Harley S. L. 1995. Partial melting and phase relations in high-grade metapelites: An experimental petrogenetic grid in the KFMASH system. *Contributions to Mineralogy and Petrology* 120:270–291.
- Degenhardt J. J., Buchanan P. C., Reid A. M., and Miller R. M. 1994. Breccia veins and dykes associated with the Roter Kamm crater, Namibia. In *Large meteorite impacts and planetary evolution*, edited by Dressler B. O., Grieve, R. A. F., and Sharpton V. L. GSA Special Paper 293. Boulder: Geological Society of America. pp. 197–208.
- Degenhardt J. J., Reid A. M., Miller R. McG., and Reimold W. U. 1996. Breccias resembling melt bombs from the Roter Kamm crater, Namibia. *Meteoritics & Planetary Science* 31:413–415.
- Engelhardt W. v., Arndt J., Fecker B., and Pankau H. G. 1995. Suevite breccia from the Ries crater, Germany: Origin, cooling history, and devitrification of impact glasses. *Meteoritics & Planetary Science* 30:279–293.
- Fudali R. F. 1973. Roter Kamm: Evidence for an impact origin. *Meteoritics & Planetary Science* 8:245–257.
- Grant J. A., Koeberl C., Reimold W. U., and Schultz P. H. 1997. Gradation of the Roter Kamm impact crater, Namibia. *Journal of Geophysical Research (Planets)* 102:16,327–16,338.
- Jarosewich E. J., Nelen J. A., and Norberg J. A. 1980. Reference samples for electron microprobe analysis. *Geostandards Newsletters* 4:43–47.
- Jourdan F., Renne P. R., and Reimold W. U. 2007a. The problem of inherited  $^{40}\text{Ar}^*$  in dating impact glass by the  $^{40}\text{Ar}/^{39}\text{Ar}$  method: Evidence from the Tswaing crater (South Africa). *Geochimica et Cosmochimica Acta* 71:1214–1231.
- Jourdan F., Renne P. R., and Reimold W. U. 2007b. Considerations in dating impact craters using the  $^{40}\text{Ar}/^{39}\text{Ar}$  method: The problem of inherited  $^{40}\text{Ar}^*$  (abstract). *Geochimica et Cosmochimica Acta* 71: A452.
- Jourdan F., Renne P. R., and Reimold W. U. 2007c. High-precision  $^{40}\text{Ar}/^{39}\text{Ar}$  age of the Jänisjärvi impact structure (Russia). *Earth and Planetary Science Letters* 265:438–449.
- Kelley S. P. 2007. The geochronology of large igneous provinces, terrestrial impact craters, and mass extinctions on Earth. *Journal of the Geological Society of London* 164:923–936.
- Kelley S. P. and Gurov E. 2002. Boltys, another end-Cretaceous impact. *Meteoritics & Planetary Science* 37:1189–1201.
- Kenkmann T., Artemieva N. A., and Poelchau M. H. 2008. The Carancas event on September 15, 2007: Meteorite fall, impact conditions, and crater characteristics (abstract #1094). 39th Lunar and Planetary Science Conference. CD-ROM.
- Koeberl C. 1993. Instrumental neutron activation analysis of geochemical and cosmochemical samples: A fast and proven method for small samples analysis. *Journal of Radioanalytical and Nuclear Chemistry* 168:47–60.
- Koeberl C. 1998. Identification of meteoritic components in impactites. In *Meteorites: Flux with time and impact effects*, edited by Grady M. M., Hutchison R., McCall G. J. H., and Rothery D. A. Geological Society of London Special Publication 140. pp. 133–153.
- Koeberl C. and Huber H. 2000. Optimization of the multiparameter  $\gamma\text{-}\gamma$  coincidence spectrometry for the determination of iridium in geological materials. *Journal of Radioanalytical and Nuclear Chemistry* 244:655–660.
- Koeberl C., Fredriksson K., Goetzinger M., and Reimold W. U. 1989. Anomalous quartz from the Roter Kamm impact crater, Namibia: Evidence for post impact hydrothermal activity? *Geochimica et Cosmochimica Acta* 53:2113–2118.
- Koeberl C., Hartung J. B., Kunk M. J., Klein J., Matsuda J. I., Nagao K., Reimold W. U., and Storzer D. 1993. The age of the Roter Kamm impact crater, Namibia: Constraints from  $^{40}\text{Ar}$ - $^{39}\text{Ar}$ , K-Ar, Rb-Sr, fission track, and  $^{10}\text{Be}$   $^{26}\text{Al}$  studies. *Meteoritics* 28:204–212.
- Koeberl C., Peucker-Ehrenbrink B., Reimold W. U., Shukolyukov A., and Lugmair G. W. 2002. Comparison of Os and Cr isotopic methods for the detection of meteoritic components in impactites: Examples from the Morokweng and Vredefort impact structures, South Africa. In *Catastrophic events and mass extinctions: Impacts and beyond*, edited by Koeberl C. and MacLeod K. G. Geological Society of America Special Paper 356. pp. 607–617.

- Koeberl C., Shukolyukov A., and Lugmair G. W. 2007. Chromium isotopic studies of terrestrial impact craters: Identification of meteoritic components at Bosumtwi, Clearwater East, Lappajärvi, and Rochechouart. *Earth and Planetary Science Letters* 256:534–546.
- Ludwig K. 2002. Isoplot/Ex version 2.49. A geochronological toolkit for Microsoft Excel. Berkeley Geochronological Center Special Publication.
- McDonald I. 2002. Clearwater East structure: A re-interpretation of the projectile type using new platinum-group element data from meteorites. *Meteoritics & Planetary Science* 37:459–464.
- McDonald I., Andreoli M. A. G., Hart R. J., and Tredoux M. 2001. Platinum-group elements in the Morokweng impact structure, South Africa: Evidence for the impact of a large ordinary chondrite projectile at the Jurassic-Cretaceous boundary. *Geochimica et Cosmochimica Acta* 65:113–123.
- McDonough W. F. and Sun S. S. 1995. The composition of the Earth. *Chemical Geology* 120:223–253.
- Montel J.-M. and Vielzeuf D. 1997. Partial melting of metagreywackes, Part II. Compositions of minerals and melts. *Contributions to Mineralogy and Petrology* 128:176–196.
- Onstott T.C., Hargraves R. B., Joubert P., and Reid D. L. 1986. Constraints on the tectonic evolution of the Namaqua Province I, Palaeomagnetic, and  $^{40}\text{Ar}/^{39}\text{Ar}$  results from the Richtersveld subprovince. *Transactions of the Geological Society of South Africa* 89:117–142.
- Peucker-Ehrenbrink B. and Jahn B.-M. 2001. Rhenium-osmium isotope systematics and platinum group element concentrations: Loess and the upper continental crust. *Geochemistry Geophysics Geosystems* 2, doi: 10.1029/2001GC000172.
- Plessen H.-G. and Erzinger J. 1998. Determination of the platinum-group elements and gold in twenty rock reference materials by inductively coupled plasma-mass spectrometry (ICP-MS) after pre-concentration by nickel sulfide fire assay. *Geostandards Newsletter* 22:187–194.
- Rajmon D., Copeland P., and Reid A. M. 2005. Argon isotopic analysis of breccia veins from the Roter Kamm crater, Namibia, and implications for their thermal history. *Meteoritics & Planetary Science* 40:841–854.
- Reimold W. U. 2007. The Impact Cratering Bandwagon (Some problems with the terrestrial impact cratering record). *Meteoritics & Planetary Science* 42:1467–1472.
- Reimold W. U. and Miller R. McG. 1989. The Roter Kamm crater, SWA/Namibia. Proceedings, 19th Lunar and Planetary Science Conference. pp. 711–732.
- Reimold W. U., Koeberl C., and Bishop J. 1994. Roter Kamm impact crater, Namibia: Geochemistry of basement rocks and breccias. *Geochimica et Cosmochimica Acta* 58:2689–2710.
- Reimold W. U., Koeberl C., and Brandt D. 1997. Suvite from the Roter Kamm impact crater, Namibia. *Meteoritics & Planetary Science* 32:431–437.
- Reimold W. U., Kelley S. P., Sherlock S. C., Henkel H., and Koeberl C. 2005. Laser argon dating of melt breccias from the Siljan impact structure: Implications for possible relationship to Late Devonian extinction events. *Meteoritics & Planetary Science* 40:591–607.
- Renne P. R., Swisher C. C., Deino A. L., Karner D. B., Owens T. L. 1998. Intercalibration of standards, absolute ages, and uncertainties in  $^{40}\text{Ar}/^{39}\text{Ar}$  dating. *Chemical Geology* 145:117–152.
- Schmitt R. T., Wittmann A., and Stöffler D. 2004. Geochemistry of drill core samples from Yaxcopoil-1, Chicxulub impact crater, Mexico. *Meteoritics & Planetary Science* 39:979–1001.
- Sherlock S. C., Kelley S. P., Parnell J., Lee P., Osinski G. R., and Cockell C. S. 2005. An Eocene Ar-Ar age for the Haughton impact structure. *Meteoritics & Planetary Science* 40:591–607.
- Skjerlie K. P., Patino Douce A. E., and Johnston A. D. 1993. Fluid absent melting of a layered crustal protolith: Implications for the generation of anatectic granites. *Contributions to Mineralogy and Petrology* 114:365–378.
- Son T. H. and Koeberl C. 2005. Chemical variation within fragments of Australasian tektites. *Meteoritics & Planetary Science* 40: 805–815.
- Stöffler D. and Langenhorst F. 1994. Shock metamorphism of quartz in nature and experiment: I. Basic observation and theory. *Meteoritics* 29:155–181.
- Tagle R. and Claeys P. 2005. An ordinary chondrite as impactor for the Popigai crater, Siberia. *Geochimica et Cosmochimica Acta* 69:2877–2889.
- Tagle R. and Hecht L. 2006. Geochemical identification of projectiles in impact rocks. *Meteoritics & Planetary Science* 41:1721–1735.
- Tagle R. and Berlin J. 2008. A database of chondrite analyses including platinum group elements, Ni, Co, Au, and Cr: Implications for the identification of chondritic projectiles. *Meteoritics & Planetary Science* 43:541–559.
- Taylor S. R. and McLennan S. M. 1985. The continental crust: Its composition and evolution. Oxford: Blackwell Scientific. 312 p.
- Taylor S. R. and McLennan S. M. 1995. The geochemical evolution of the continental crust. *Reviews of Geophysics* 33:241–265.
- Villaseca C., Orejana D., Paterson B. A., Billstrom K., and Pérez-Soba C. 2007. Metaluminous pyroxene-bearing granulite xenoliths from the lower continental crust in central Spain: Their role in the genesis of Hercynian I-type granites. *European Journal of Mineralogy* 19:463–477.
- Wedepohl K. H. 1995. The composition of the continental crust. *Geochimica et Cosmochimica Acta* 59:1217–1232.
-